Journal of Materials Chemistry A

RSC Publishing

PAPER

View Article Online
View Journal | View Issue

Cite this: J. Mater. Chem. A, 2013, 1, 12088

The influence of 1D, meso- and crystal structures on charge transport and recombination in solid-state dye-sensitized solar cells†

Pablo Docampo,[a] Aruna Ivaturi,[b] Robert Gunning,[a] Sandra Diefenbach,[c] James Kirkpatrick,[a] Claudia M. Palumbiny,[c] Varun Sivaram,[a] Hugh Geaney,[d] Lukas Schmidt-Mende,[ce] Mark E. Welland[b] and Henry J. Snaith*[a]

We have prepared single crystalline SnO_2 and ZnO nanowires and polycrystalline TiO_2 nanotubes (1D networks) as well as nanoparticle-based films (3D networks) from the same materials to be used as photoanodes for solid-state dye-sensitized solar cells. In general, superior photovoltaic performance can be achieved from devices based on 3-dimensional networks, mostly due to their higher short circuit currents. To further characterize the fabricated devices, the electronic properties of the different networks were measured *via* the transient photocurrent and photovoltage decay techniques. Nanowire-based devices exhibit extremely high, light independent electron transport rates while recombination dynamics remain unchanged. This indicates, contrary to expectations, a decoupling of transport and recombination dynamics. For typical nanoparticle-based photoanodes, the devices are usually considered electron-limited due to the poor electron transport through nanocrystalline titania networks. In the case of the nanowire-based devices, the system becomes limited by the organic hole transporter used. In the case of polycrystalline TiO_2 nanotube-based devices, we observe lower transport rates and higher recombination dynamics than their nanoparticle-based counterparts, suggesting that in order to improve the electron transport properties of solid-state dye-sensitized solar cells, single crystalline structures should be used. These findings should aid future design of photoanodes based on nanowires or porous semiconductors with extended crystallinity to be used in dye-sensitized solar cells.

Received 10th May 2013
Accepted 13th August 2013

DOI: 10.1039/c3ta11855j

www.rsc.org/MaterialsA

Introduction

The dye-sensitized solar cell (DSCs)[1] is a very attractive low-cost system that can potentially deliver solar cells with comparable power conversion efficiencies to some of the current thin film inorganic devices for a fraction of the cost. DSCs are composed of a transparent conductive oxide (TCO), typically fluorine doped tin oxide, over which a mesoporous layer of a metal oxide is deposited, usually anatase TiO_2. This mesostructure is then sensitized with a light absorbing dye, filled with a hole transport medium, typically a redox active electrolyte, and finally capped with a regenerating top contact, generally platinum. Photovoltaic action arises from photoexcited electrons in the sensitizer, which are transferred to the conduction band (CB) of the metal oxide and then transported through the mesostructure to the TCO. Meanwhile, holes on the dye molecules are regenerated by the electrolyte which then diffuse through to the platinum counter-electrode.

Utilizing liquid electrolytes leads to significant technological challenges, since the devices must be carefully sealed to avoid leaks. Furthermore, the archetypal iodide triiodide redox couple is corrosive. In order to address these issues, in 1998 Bach *et al.*[2] replaced the liquid electrolyte with an organic solid-state alternative, 2,2′,7,7′-tetrakis-(*N*,*N*-di-*p*-methoxyphenylamine)-9,9′(-spirobifluorene) spiro-OMeTAD.[3] Beyond technical advantages, a lower "over-potential" should be required to regenerate holes in the dye by using the solid state hole transporting material (HTM) since it is only a one step process, whereas two or more steps are generally required when dealing with iodide/triiodide. This loss minimization promises to lead to non-trivial higher achievable power conversion efficiencies for the solid-state based devices.[4,5]

The power conversion efficiency of complete devices depends on light absorption, charge generation and charge collection efficiencies. Charge generation efficiency depends on

[a]Clarendon Laboratory, University of Oxford, Parks Road, Oxford, OX1 3PU, UK. E-mail: h.snaith1@physics.ox.ac.uk

[b]Nanoscience Centre, Department of Engineering, University of Cambridge, 11 J J Thomson av., Cambridge CB3 0FF, UK

[c]Department of Physics and Center for NanoScience, Amalienstr. 54, 80799 München, Germany

[d]MSSI, Department of Chemical and Environmental Science, University of Limerick, Ireland

[e]Department of Physics, University of Konstanz, 78457 Konstanz, Germany

† Electronic supplementary information (ESI) available. See DOI: 10.1039/c3ta11855j

the intrinsic electron transfer properties of a particular dye and on the regeneration of the dye from the redox couple in the electrolyte. Light absorption efficiency is high if the active layer of a device is thick enough to absorb enough light. Charge collection efficiency depends on the balance of diffusion and recombination in a device. A particularly important quantity is the electron diffusion length (D_L) defined as $D_L = \sqrt{D_e \tau}$, where D_e is the diffusion coefficient and τ the recombination lifetime.

Only charges generated within an electron diffusion length of the electron contact can be collected efficiently, and in fact, the film has to be approximately 3 times thinner than the diffusion length to achieve 99% collection efficiency. Therefore the strategy necessary to design a high power conversion efficiency device is to ensure that the electron diffusion length is long compared to the light absorption length, thereby guaranteeing simultaneously high charge collection and light absorption efficiencies.

The charge transport in mesoporous metal oxide films is usually described by a multiple trapping process, where most of the electrons are trapped in localised sub band gap states, and only charges thermally populating the conduction band are free to move. In addition, the original theories for multi-trapping transport *and recombination* in DSCs stipulate that only the free electrons can take part in recombination between the electrons in the TiO_2 and holes in the hole-transporter.[6,7] This leads to an interdependency of recombination upon transport, and potentially presents a fundamental limitation to increasing the diffusion length *via* increasing the transport rate.

In practice, the theoretical increases in efficiencies promised by using solid hole-transport materials have not yet been realized. This is in part because the recombination processes are significantly faster in solid hole transporter based devices than in liquid electrolyte DSCs, leading to significantly shorter electron recombination lengths and open-circuit voltages lower than possible, and hence to lower power conversion efficiencies.[8,9] This limits the active layer thickness for the best performing devices to about ~2.5 μm, seriously reducing the device performance due to poor light absorption in the red region of the spectrum.[10] Even though recent research has shown that pore filling by the solid HTM can be achieved for films of over 5 μm,[11,12] such devices do not lead to increased PCE, in part due to poor charge collection efficiencies.[13] We note that additional losses due to parasitic absorption primarily from the doped hole-conductor are also present which would need to be addressed for full efficiency to be achieved.[14]

Increasing the electron recombination length is therefore an important task to maximise all the photovoltaic parameters; short-circuit current, fill factor and open-circuit voltage. This can be achieved either by increasing the diffusion coefficient or by reducing the recombination rate. In principle, diffusion coefficients could be increased by using photoanodes fabricated from metal oxides with higher bulk mobility than titania, for example zinc oxide or tin oxide, since charge transport in these systems is linked to the free electrons in the conduction band. Alternatively, photoanodes fabricated using materials with bigger crystallite sizes can also deliver faster transport kinetics.[15] Recombination rates might be reduced by encasing the nanocrystals with a thin insulating oxide coating.[16–20]

Another approach to improve the transport through the films incorporates 1-dimensional nanostructrures, *i.e.* nanowires, in the photoanode design.[21–24] The most salient feature of devices fabricated from highly crystalline nanowires is much faster electron transport as compared to standard nanoparticle-based photoanodes.[22] Though we note that due to the nature of the multiple trapping mechanism and *diffusion limited recombination*[6,25] it is uncertain that simply enhancing the transport rate would have the desired beneficial impact upon diffusion length.

In this article we aim to clarify the global influence of 1D structured metal oxide photoanodes upon charge transport, recombination and hence diffusion length in solid-state dye-sensitized solar cells. The two type of 1D systems extensively developed are nanowire arrays grown directly on a substrate and nanotube arrays which are anodized directly on a substrate. Here, we grow nanowire arrays of SnO_2 and ZnO, and nanotube arrays of TiO_2 and compare their electronic performance to standard nanoparticle-based films. We observe that electron transfer rates through the nanowire based devices are orders of magnitude faster than the standard nanoparticle devices, however, the TiO_2 nanotube-based devices exhibit around 10 fold slower transport than the standard nanoparticle based devices. In contrast, when single crystalline TiO_2 nanowires are used,[26] fast and bias-independent transport is achieved. This leads us to conclude that the long range crystallinity of the nanowires, which is not present in the nanotubes, is critical for achieving enhanced transport since grain boundaries have been eliminated.[27] Notably, the recombination in the nanowire based devices is no faster than in the standard nanoparticle films, indicating a predominant "decoupling" of transport and recombination, in contrast to predictions from conventional theories.

Results and discussion

The ZnO nanowires used in this study were grown hydrothermally on fluorine doped tin oxide (FTO) substrates (pre-coated with a sputtered Zn compact layer) using a mixture of zinc nitrate hydrate and hexamethylenetetramine in water at low temperatures (92 °C).[28,29] The as grown nanowires were predominantly single crystalline with an average length of ~500 nm and ~30 nm width. SnO_2 nanowires were grown hydrothermally using a mixture of tin chloride pentahydrate, urea and hydrochloric acid in water at low temperatures (95 °C),[30] resulting in nanowires with an average length of ~200 nm and ~50 nm diameter. TiO_2 nanotubes were grown by anodization of titanium metal which was pre-sputtered on an indium doped tin oxide (ITO) substrate, in the presence of ammonium fluoride in ethylene glycol.[31] The nanotubes were ~1.3 μm thick, and with a wall thickness of ~20 nm. A cross section of all the nanostructures is shown in Fig. 1(a–c). X-ray diffraction measurements (see ESI†) confirm the predominantly single crystalline nature of the SnO_2 and ZnO. In the case of TiO_2 nanotubes, a crystallite size of ~35 nm was estimated.

For all devices we matched the thickness of the 1D electrodes to the thickness of the standard nanoparticle based anodes in

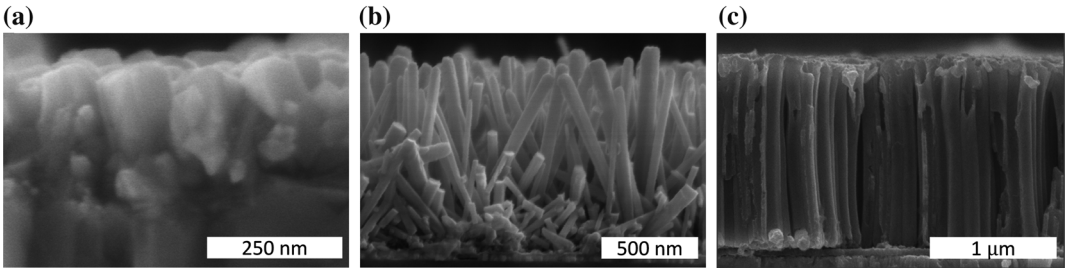

Fig. 1 Scanning electron microscope images of a cross section of (left) SnO_2 nanowires, (center) ZnO nanowires, and (right) TiO_2 nanotubes.

order to make a fair comparison in the transport studies. The photovoltaic performance of the fabricated devices is shown in Fig. 2 and all photovoltaic parameters are summarized in Table 1. In all cases, the devices fabricated from nanoparticle-based photoanodes show higher short-circuit currents than their nanowire/nanotube counterparts. This is consistent with the less available surface area present in the nanowire films. In the case of the SnO_2 and ZnO nanowires, a significant improvement in the fill factor is also observed as compared with the nanoparticle-based devices fabricated from the same materials. In the case of TiO_2 nanotubes, an open circuit voltage which is 100 mV lower than the nanoparticle-based devices is observed as well as a significantly lower fill factor. This is indicative of higher recombination or slower transport or a combination of both present in the nanotube system.

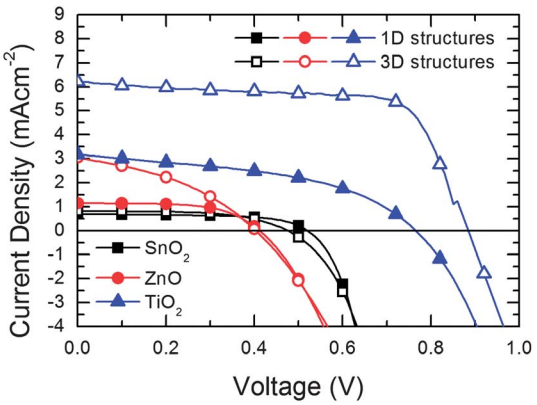

Fig. 2 Current–voltage curves for devices fabricated from SnO_2 (black squares), ZnO (red circles) and TiO_2 (blue triangles). Closed symbols refer to 1D structures, open symbols to 3D nanoparticle based films.

Table 1 Summary of the photovoltaic parameters for all 1D and 3D structures of the *JV* curves shown in Fig. 2. NP refers to nanoparticles, NW to nanowires and NT to nanotubes

	J_{sc} (mA cm^{-2})	η (%)	V_{oc} (V)	FF
ZnO NW	0.98	0.27	0.39	0.71
SnO_2 NW	0.97	0.35	0.59	0.61
TiO_2 NT	3.18	1.12	0.77	0.46
ZnO NP	2.99	0.61	0.58	0.35
SnO_2 NP	0.81	0.31	0.63	0.60
TiO_2 NP	6.81	3.72	0.85	0.64

It is also important to measure the electronic properties of the grown structures. A technique used to achieve this is to perform transient experiments where a small light perturbation is applied to the cell under operation and its response is measured. If the experiment is carried out at a fixed potential, the time it takes for the photocurrent transient to decay can be directly related to the diffusion of electrons whereas if it is carried out at constant current, the extra charge generated cannot leave the device through the contacts and the photovoltage transient time is related to the recombination time. Further details can be found in the Experimental section.

The charge transport properties of the different structures are presented in Fig. 3. Both the SnO_2 and ZnO nanowire-based devices exhibit similar "light-intensity-independent" transport rates of $\sim 4 \times 10^4$ s^{-1}. A similar result was found by Tetrault *et al.* in single crystalline TiO_2 nanowire photoanodes, where transport rates were found to be independent of the bias applied.[26] In contrast, nanoparticle devices (*i.e.* 3D networks) lie over one order of magnitude below them and exhibit the expected light intensity dependence with enhanced transport at higher background light intensities due to the filling of traps. TiO_2 nanotube-based devices exhibit uncharacteristically low light intensity-dependent transport rates, several orders of magnitude slower than devices fabricated from nanoparticles of a similar thickness, consistent with a larger density of trap sites.

In opposition to expectations from transport-limited recombination models, the recombination rates for 3-dimensional networks are generally similar to or higher than those exhibited by the nanowire-based devices. Indeed, when comparing the ZnO electrodes at high light biases (full sun, 100 mW cm^{-2}), the ZnO nanowire devices exhibit around one order of magnitude lower recombination rates than the nanoparticle-based counterparts. The simplest interpretation of these results is that recombination occurs not only from free electrons, but also from electrons trapped in surface states; the latter effect is possibly predominant.[32,33] Hence, the more crystalline nanowires have fewer available surface states through which recombination can occur, and thus slower recombination rates. Alternatively, we can hypothesize that recombination is only strongly related to the quasi Fermi level of electrons in the oxide and not to the diffusion coefficient. Regardless, simply observing the trend of faster transport and slower

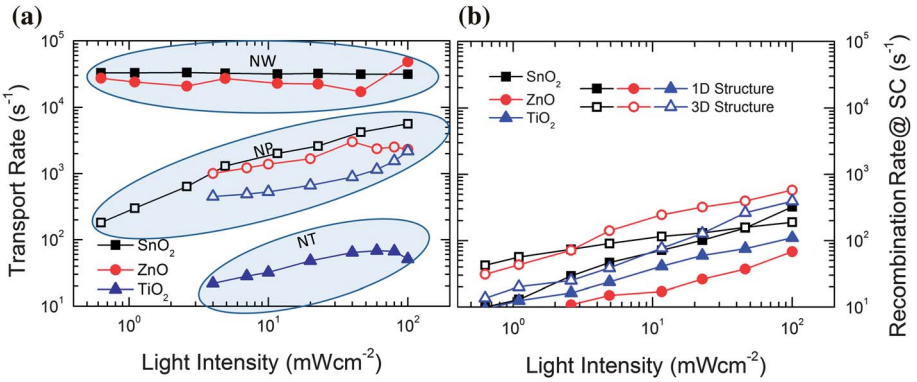

Fig. 3 Transport rates (a) and recombination rates at short circuit (b) against light intensity for devices fabricated from SnO_2 (black squares), ZnO (red circles) and TiO_2 (blue triangles). Closed symbols refer to 1D structures, open symbols to 3D nanoparticle based films.

recombination is greatly encouraging since it unambiguously demonstrates that transport and recombination can be independently optimised. Devices based on TiO_2 nanotubes on the other hand exhibit higher recombination rates at high biases than their nanoparticle-based counterparts, which explains the significantly lower open circuit voltages observed in Fig. 2,[34] suggesting that a high trap density is present in this system. This is intriguingly consistent with the slower transport under the assumption that recombination is predominantly mediated through surface states.

Generally, transport through the nanocrystalline titania used in DSCs is described as a trapping and detrapping process. Trapping time is proportional to the trap depth and the fraction of charge which is trapped or free depends on the relative density of states at the Fermi level and in the conduction band. Hence as the Fermi level rises, the thermal population in the conduction band increases along with its fractional population and thus the transport rate.[35–39] For the nanowire-based devices used in this study, transport rates are relatively independent of the light intensity incident on the solar cell, in stark contrast to nanoparticle based devices. This suggests that either charge trapping–detrapping processes are no longer dominating the diffusion of charges through the nanowires, or the ambipolar diffusion is no longer limited by electron transport, but is rather limited by hole-transport.

The ambipolar diffusion coefficient (D_{amb}) is what is really determined in the transient measurements. It is related to the electron and hole diffusion coefficient (D_n and D_p) and the electron and hole number density (n and p) *via* the following relationship:[38,40]

$$D_{amb} = \frac{n+p}{\frac{n}{D_p}+\frac{p}{D_n}} \quad (1)$$

Hence, if either the hole number density is higher or the hole diffusion coefficient is faster, then the system will be governed by electron transport and $D_{eff} \sim D_n$. For the electrolyte DSC, the concentration of ions in the electrolyte is so high that although D_p is low, the transport is still more or less limited by electron diffusion. For the solid-state DSC, the hole-transporter is partially oxidized, increasing p, and, additionally, the mobility of holes in spiro-OMeTAD is suitably high that at short-circuit where electron transport is slow the conventional system is still limited by electron transport. It is therefore likely that by enhancing the electron diffusion coefficient with the employment of the nanowires, the system has now become limited by the hole-diffusion in spiro-OMeTAD.

To verify this, we have constructed devices consisting of a flat compact layer of ZnO of ~10–20 nm in thickness deposited over the FTO, sensitized with the same D102 dye and coated *via* spincoating with different thicknesses of the hole transporting material. In this configuration, the electron–hole pairs are generated very close to the electrode and hole dynamics are expected to dominate. The transport properties of the devices were then measured *via* the photovoltage and photodecay techniques and the results are shown in Fig. 4. Here, it can be observed that charge transport in these devices is also light intensity independent and lies within the same range as the nanowire devices presented in Fig. 3. It is clear then that the transport characteristics shown in Fig. 2 correspond to devices which are "hole-limited", and hence the transport rates shown represent a lower bound to the electron transport through the nanowires.

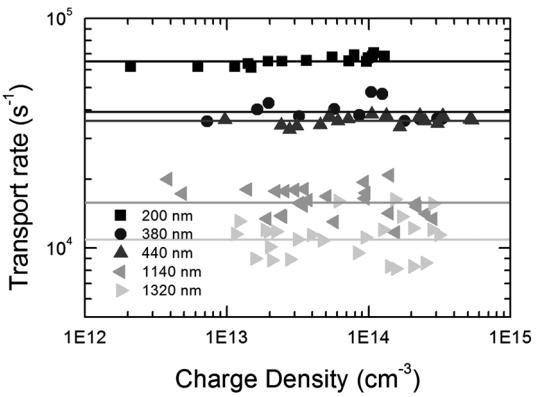

Fig. 4 Transport rates plotted against charge density for flat layer devices consisting of a dye-sensitized ZnO compact layer of ~20 nm in thickness for a range of spiro-OMeTAD thicknesses estimated from SEM cross-sectional images (see ESI†). Points shown correspond to at least 3 different devices. Flat lines correspond to the average of the measured data points.

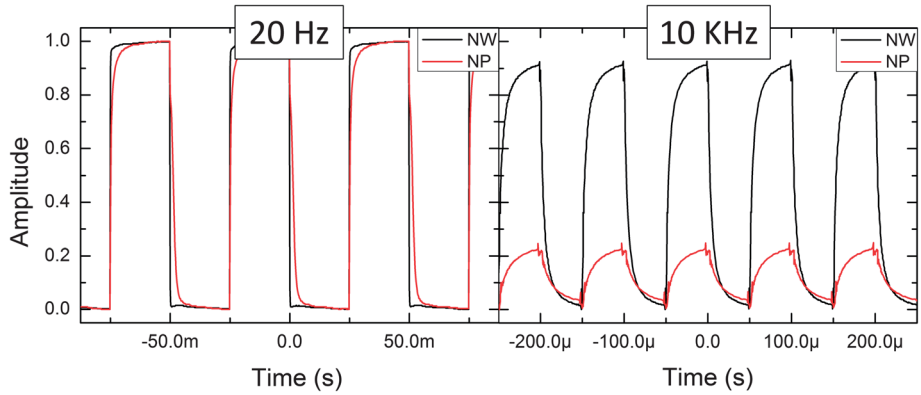

Fig. 5 Normalized to 5 Hz signal photocurrent response to a square light pulse with no background bias or light for devices fabricated from nanowires (NW, black line) and nanoparticles (NP, red line) based on Y_2O_3 covered SnO_2.

While the precise diffusion length of the nanowire devices fabricated in this study cannot be determined due to the hole-limited nature of their transport, a minimum value can be extracted from the photovoltage and photocurrent decay measurements. For ZnO nanowires we have estimated diffusion lengths of at least 8 μm and 4.5 μm for those based on SnO_2. In contrast, nanoparticle based devices fabricated from the same materials resulted in diffusion lengths of about 1 μm. We estimate very poor diffusion lengths of ~0.5 μm for devices fabricated from TiO_2 nanotubes, while their nanoparticle-based counterparts show values of over 2 μm. The longer diffusion lengths estimated here for the nanowire based devices is in very good agreement with a recent paper by Xu *et al.*; who have demonstrated that extremely thick 50 μm ZnO nanowire arrays can be employed as very effective photoanodes in solid-state DSCs, delivering over 5% solar power conversion efficiency.[24]

Our transport and X-ray data strongly indicates that it is not enough to have a 1D mesostructure, with the intention to shorten the travel distance for electron to the electrodes to achieve faster transport in dye-sensitized solar cells, as previously noted by Yang *et al.*[10] Indeed, other groups report similar diffusion coefficients for TiO_2 nanotube and nanoparticle-based devices with similar crystallite size (similar to the ones used in this study ~30 nm)[41] and only when the crystallite sizes are considerably different are transport properties affected strongly.[42] Taking all this evidence into account, it seems that in order to achieve fast diffusion coefficients, and hence long diffusion lengths, it is absolutely necessary to work with extended and preferably single crystalline systems.

Beyond solar cell applications, the solid-state dye-sensitized solar cells based on SnO_2 and ZnO nanowires presented in this study have extremely fast transport rates and may fulfil the requirements for high-speed photodetectors, which typically require switching speeds in the kHz range. To see whether this is the case, we have measured the photoresponse of the SnO_2 cells with a 10 kHz signal, after previously normalizing the response to a 20 Hz signal (see Fig. 5). We can clearly see that the nanowire devices follow the incident light at this high frequency, only losing about ~10% of the signal strength. In comparison, nanoparticle based devices lose ~80% of the signal. We note that faster switching speeds should easily be possible with other hole transporting materials with faster mobilities than spiro-OMeTAD, such as P3HT.[43–45] This is a very promising result since dye-sensitized solar cells can be very easily tuned to the required absorption bandwidth without changing the metal oxide. This can be achieved by simply changing the adsorbed dye, thus, leaving the transport properties unaffected.

Conclusions

We have prepared predominantly single crystalline SnO_2 and ZnO nanowires and polycrystalline TiO_2 nanotubes as photoanodes for solid-state dye-sensitized solar cells. Nanowire-based devices exhibit extremely high, light independent transport rates, consistent with the electron diffusion being so fast that the devices have become "hole-limited" under short-circuit conditions, rather than electron-limited as is the case in devices fabricated from nanoparticle assemblies. TiO_2 nanotubes exhibit lower transport rates and higher recombination dynamics than their nanoparticle-based counterparts. This suggests that in order to improve the transport properties of solid-state dye-sensitized solar cells, extended or single crystalline structures should be employed. Notably, this study has clearly demonstrated a lack of correlation between changes in transport and changes in recombination rates when comparing the standard nanoparticle based films to the 1D nanostructures. This decoupling indicates that there is extensive scope to enhance the charge collection efficiency and diffusion length without unintended consequences through enhanced recombination in dye-sensitized and mesostructured solar cells.

Experimental

SnO_2 and ZnO photoanode preparation

Fluorine doped tin oxide (FTO) coated glass sheets (15 Ω $\square^{-1}$ Pilkington) were etched with zinc powder and HCl (2 molar) to obtain the required electrode pattern. The sheets were then washed with soap (2% Hellmanex in water), de-ionized water, acetone, methanol and finally treated under an oxygen plasma for 10 minutes to remove the last traces of organic residues. The

FTO sheets were then sputtered with a SnO_2 target, for the SnO_2-based devices and Zn for the ZnO-based devices to achieve a compact layer thickness of 100 nm.

The ZnO nanowires were hydrothermally grown in a mixture of 0.025 M zinc nitrate hydrate and 0.025 M hexamethylenetetramine (HMT) in water.

The SnO_2 nanowires were hydrothermally grown in a 0.0001 M $SnCl_4 \cdot 5H_2O$, 0.15 M urea and 0.6 M HCl mixture in water.

For both materials, the growth was carried directly by submerging the respective compact layer-coated FTO substrates into their growth solution, which was then kept at a temperature of 92 °C for 120 min for the ZnO nanowires and over 24 h for the SnO_2 nanowires.

For the SnO_2 nanoparticle-based devices a home-made mesoporous paste was prepared in a similar way as Ito *et al.*[46] from <100 nm particle size SnO_2 nanopowder (549657 Sigma-Aldrich).

For the ZnO nanoparticle-based devices a home-made mesoporous paste was prepared by mixing ZnO nanoparticles 40 wt% in ethanol (721085 Sigma-Aldrich) with terpineol (anhydrous, Sigma-Alrich), butylamine (≥99.5% Sigma-Aldrich) and a mixture of ethyl-cellulose 10 wt% in ethanol.

First, a 1 : 1 by weight mixture of ethyl cellulose with different viscosities (5–15 mPa s, 46070 Sigma and 30–70 mPa s, 46080 Sigma) was added slowly into ethanol while under vigorous stirring to achieve a final concentration of 10 wt%.

Then, for every gram of the ZnO dispersion, 0.83 ml of butylamine and 2.5 g of terpineol were mixed, stirred and sonicated for 30 s with an ultrasonic horn. After this step, 3.75 g of the ethyl cellulose mixture in ethanol were added, stirred and sonicated for 30 s. After sonication, ethanol was completely removed from the paste *via* rotary evaporation.

For both materials, the respective pastes were doctor bladed by hand using scotch tape and a pipette on their corresponding metal-oxide covered FTO sheets.

Nanoparticle-based SnO_2 structures were then slowly heated (ramped over 1½ hours) to 500 °C and kept at this temperature for 30 minutes, while the ZnO nanoparticle-based films were heated with a similar ramp rate to 400 °C and kept at this temperature for 30 minutes. After cooling, all substrates (nanoparticle and nanowire-based) were cut down to size and soaked in a 10 mM yttrium nitrate hexahydrate and 40 mM sodium hydroxide aqueous solution for the SnO_2-based devices and a 25 mM magnesium nitrate hexahydrate and 40 mM sodium hydroxide aqueous solution for ZnO-based devices, for 15 min on a hot plate set at 150 °C. After rinsing with deionized water and drying in air, the electrodes were subsequently baked once more at 500 °C for the SnO_2-based devices and 400 °C for the ZnO-based devices, for 45 min in air, then cooled down to 70 °C.

TiO_2-based photoanode preparation

For TiO_2 nanotubes, ITO covered glass substrates (Kintech; 10 $\Omega\ \square^{-1}$) were cleaned with commercial dishwashing detergent using an ultrasonic toothbrush. Subsequently, the ITO substrates were ultrasonicated for 15 min each in acetone and 2-propanol, rinsed with ethanol, and dried in a nitrogen stream. Prior to loading the sputter system, 7 min oxygen plasma cleaning was performed. Approximately 50 nm of TiO_2 and 1 μm of Ti were DC sputtered at 500 °C with a Surrey Nano-Systems Gamma 1000C sputter system at Ar pressures of 5 mTorr and 4 mTorr, respectively. Subsequently, the substrates were allowed to slowly cool down in high vacuum.

Anodization was carried out using a two electrode setup with a Pt counter electrode in an ethylene glycol bath containing 0.4 wt% NH_4F (Sigma Aldrich). 2 vol% pure water was added and the solution was stirred for at least 1 h in ambient air prior to anodization. Samples were anodized at 300 K, with an anodization voltage of 60 V for about 2 min, until the anodization current–time reached its second dip as established in a previous publication.[31] Anodizations were carried out at room temperature on 1 μm Ti samples. After anodization the samples were rinsed with water and ethanol and dried in air. A heat curing was performed at 450 °C for 1 h with heating and cooling rates of 3 °C min^{-1} in ambient atmosphere.

For nanoparticle-based TiO_2 photoanodes, indium doped tin oxide (ITO) coated glass sheets (15 $\Omega\ \square^{-1}$ Pilkington) were etched with zinc powder and HCl (2 molar) to obtain the required electrode pattern. The sheets were then washed with soap (2% Hellmanex in water), de-ionized water, acetone, methanol and finally treated under an oxygen plasma for 10 minutes to remove the last traces of organic residues. The ITO sheets were subsequently coated with a compact layer of TiO_2 (100 nm) by aerosol spray pyrolysis deposition of titanium diisopropoxide bis(acetylacetonate) (Sigma-Aldrich) mixed with ethanol in a 1 : 10 precursor : ethanol ratio at 450 °C using air as the carrier gas. A commercially available nanoparticle paste (Dyesol NR-18T), diluted with ethanol, was spincoated directly on the substrate, achieving ~1 μm thickness at 2000 rpm. The substrates were then slowly heated to 450 °C (ramped over 1 hour) and baked at this temperature for 30 minutes in air. After cooling, the slides were soaked in a 15 mM $TiCl_4$ bath for 1 hour at 70 °C. After rinsing with deionized water and drying in air, the electrodes were subsequently baked once more at 450 °C for 45 min in air, and then cooled down to 70 °C.

Solid-state dye-sensitized solar cell assembly

The indoline dyes used were D102,[47] and D149 0.2 mM in a 1 : 1 volume ratio of *tert*-butanol and acetonitrile. 2,2′,7,7′-Tetrakis(*N*,*N*-di-*p*-methoxypheny-amine)-9,9′-spirobifluorene (spiro-OMeTAD) was dissolved in chlorobenzene at 10 vol% concentration and after fully dissolving the hole transporter, 4-*tert*-butyl pyridine (*t*BP) was added with a volume to mass ratio of 1 : 26 μl mg^{-1} *t*BP : spiro-OMeTAD. Lithium bis(trifluoromethylsulfonyl)-imide salt (Li-TFSI) was pre-dissolved in acetonitrile at 170 mg ml^{-1} and added to the hole transporter solution at 1 : 12 μl mg^{-1} of Li-TFSI solution : spiro-OMeTAD. The dyed films were rinsed briefly in acetonitrile and dried in air for 1 minute. For spin-coating, a small quantity of the hole transporter solution (22 μl) was dispensed onto each substrate and left to wet the films for 15 s before spin-coating at 1000 rpm for 40 s in air. The films were left overnight in an air atmosphere before placing them in a thermal evaporator where 150 nm thick silver electrodes were deposited through a shadow mask under high vacuum (10^{-6}

mbar). The active areas of the devices were defined by metal optical masks with 0.09 to 0.125 cm^2 apertures.

Solar cell characterization

Solar simulated AM 1.5 sunlight was generated with an ABET solar simulator calibrated to give 100 mW cm^{-2} using an NREL calibrated KG5 filtered silicon reference cell. The *JV* curves were recorded with a Keithley 2400. The solar cells were masked with a metal aperture defining the active area of the solar cells.

The photovoltage decay measurement was performed by a similar method to O'Regan *et al.*[48] and as described elsewhere.[13,49,50] In essence, a steady-state background white illumination from an array of diodes (Lumiled Model LXHL-NWE8 whitestar) is first applied to the cell, filling up a fraction of the available sub bandgap states which will be proportional to the intensity applied. Then, a short pulse was generated from red light diodes (LXHLND98 redstar, 200 μs square pulse width, 100 ns rise and fall time), which is irradiated on the cell and its response is recorded with an oscilloscope. The perturbation light source was set to a suitably low level such that the decay kinetics were monoexponential. This enabled the charge recombination rate constants to be obtained directly from the exponential decays measured with a 1 GHz Agilent oscilloscope. When the measurement is performed at fixed potential conditions, *i.e.* potentiostatic mode, the generated charge (ΔQ) by the pulse can be directly extracted by integrating the photocurrent decay curve. When the measurements is performed at fixed current conditions, *i.e.* galvanostatic mode, the current generated through the small perturbation pulse is not allowed to exit the device and hence the response measured with oscilloscope is purely dependent on the recombination kinetics of the system, and the perturbation voltage (ΔV) can be extracted. By doing these two measurements at either open or short circuit, we can directly measure the differential capacitance as a function of voltage for the system as $C\,(\mathrm{V}) = \Delta Q/\Delta V$.

To extract the transport lifetimes as a function of charge density, the monoexponential decay dynamics of the cells were measured in potentiostatic mode with different applied background light intensities with a suitably low perturbation pulse. The charge density was then extracted as explained below. The diffusion coefficient (D_e) can be calculated as $D_e = \frac{t^2}{2.35\tau_{trans}}$, where t is the thickness of the film,[51] and τ_{trans} is the transport lifetime at short circuit conditions.

Material characterization

SEM images of TiO_2 nanotube samples were done in an Ultra Plus field emission scanning electron microscope from Carl Zeiss SMT GmBG.

Notes and references

1 B. Oregan and M. Gratzel, *Nature*, 1991, **353**, 737–740.
2 U. Bach, D. Lupo, P. Comte, J. E. Moser, F. Weissortel, J. Salbeck, H. Spreitzer and M. Gratzel, *Nature*, 1998, **395**, 583–585.
3 H. J. Snaith and L. Schmidt-Mende, *Adv. Mater.*, 2007, **19**, 3187–3200.
4 J. N. Clifford, E. Palomares, M. K. Nazeeruddin, M. Gratzel and J. R. Durrant, *J. Phys. Chem. C*, 2007, **111**, 6561–6567.
5 H. J. Snaith, *Adv. Funct. Mater.*, 2010, **20**, 13–19.
6 N. Kopidakis, K. D. Benkstein, J. van de Lagemaat and A. J. Frank, *J. Phys. Chem. B*, 2003, **107**, 11307–11315.
7 A. J. Frank, N. Kopidakis and J. v. d. Lagemaat, *Coord. Chem. Rev.*, 2004, **248**, 1165–1179.
8 J. Kruger, R. Plass, M. Gratzel, P. J. Cameron and L. M. Peter, *J. Phys. Chem. B*, 2003, **107**, 7536–7539.
9 F. Fabregat-Santiago, J. Bisquert, L. Cevey, P. Chen, M. Wang, S. M. Zakeeruddin and M. Gratzel, *J. Am. Chem. Soc.*, 2008, **131**, 558–562.
10 M. Law, L. E. Greene, A. Radenovic, T. Kuykendall, J. Liphardt and P. D. Yang, *J. Phys. Chem. B*, 2006, **110**, 22652–22663.
11 I. K. Ding, J. Melas-Kyriazi, N.-L. Cevey-Ha, K. G. Chittibabu, S. M. Zakeeruddin, M. Gratzel and M. D. McGehee, *Org. Electron.*, 2010, **11**, 1217–1222.
12 P. Docampo, A. Hey, S. Guldin, R. Gunning, U. Steiner and H. J. Snaith, *Adv. Funct. Mater.*, 2012, **22**, 5010–5019.
13 H. J. Snaith, R. Humphry-Baker, P. Chen, I. Cesar, S. M. Zakeeruddin and M. Gratzel, *Nanotechnology*, 2008, **19**, 424003.
14 G. Y. Margulis, B. E. Hardin, I. K. Ding, E. T. Hoke and M. D. McGehee, *Adv. Energy Mater.*, 2013, **3**, 959–966.
15 K. Zhu, N. Kopidakis, N. R. Neale, J. van de Lagemaat and A. J. Frank, *J. Phys. Chem. B*, 2006, **110**, 25174–25180.
16 A. Kay and M. Gratzel, *Chem. Mater.*, 2002, **14**, 2930–2935.
17 B. C. O'Regan, S. Scully, A. C. Mayer, E. Palomares and J. Durrant, *J. Phys. Chem. B*, 2005, **109**, 4616–4623.
18 F. Fabregat-Santiago, J. Garcia-Canadas, E. Palomares, J. N. Clifford, S. A. Haque, J. R. Durrant, G. Garcia-Belmonte and J. Bisquert, *J. Appl. Phys.*, 2004, **96**, 6903–6907.
19 C. Prasittichai and J. T. Hupp, *J. Phys. Chem. Lett.*, 2010, **1**, 1611–1615.
20 P. Docampo, P. Tiwana, N. Sakai, H. Miura, L. M. Herz, T. Murakami and H. J. Snaith, *J. Phys. Chem. C*, 2012, **116**, 22840–22846.
21 S. Gubbala, V. Chakrapani, V. Kumar and M. K. Sunkara, *Adv. Funct. Mater.*, 2008, **18**, 2411–2418.
22 A. B. F. Martinson, M. r. S. Góes, F. Fabregat-Santiago, J. Bisquert, M. J. Pellin and J. T. Hupp, *J. Phys. Chem. A*, 2009, **113**, 4015–4021.
23 M. Law, L. E. Greene, J. C. Johnson, R. Saykally and P. Yang, *Nat. Mater.*, 2005, **4**, 455–459.
24 C. Xu, J. Wu, U. V. Desai and D. Gao, *Nano Lett.*, 2012, **12**, 2420–2424.
25 B. Movaghar, *J. Phys. C: Solid State Phys.*, 1980, **13**, 4915.
26 N. Tétreault, E. Horváth, T. Moehl, J. Brillet, R. Smajda, S. Bungener, N. Cai, P. Wang, S. M. Zakeeruddin, L. Forró, A. Magrez and M. Grätzel, *ACS Nano*, 2010, **4**, 7644–7650.
27 P. Docampo, S. Guldin, U. Steiner and H. J. Snaith, *J. Phys. Chem. Lett.*, 2013, **4**, 698–703.
28 N. O. V. Plank, I. Howard, A. Rao, M. W. B. Wilson, C. Ducati, R. S. Mane, J. S. Bendall, R. R. M. Louca, N. C. Greenham,

H. Miura, R. H. Friend, H. J. Snaith and M. E. Welland, *J. Phys. Chem. C*, 2009, **113**, 18515–18522.
29 N. O. V. Plank, H. J. Snaith, C. Ducati, J. S. Bendall, L. Schmidt-Mende and M. E. Welland, *Nanotechnology*, 2008, **19**, 465603.
30 L. Vayssieres and M. Graetzel, *Angew. Chem., Int. Ed.*, 2004, **43**, 3666–3670.
31 J. Weickert, C. Palumbiny, M. Nedelcu, T. Bein and L. Schmidt-Mende, *Chem. Mater.*, 2011, **23**, 155–162.
32 J. Bisquert, A. Zaban and P. Salvador, *J. Phys. Chem. B*, 2002, **106**, 8774–8782.
33 J. Nelson, S. A. Haque, D. R. Klug and J. R. Durrant, *Phys. Rev. B: Condens. Matter Mater. Phys.*, 2001, **63**, 205321.
34 H. J. Snaith, L. Schmidt-Mende, M. Gratzel and M. Chiesa, *Phys. Rev. B: Condens. Matter Mater. Phys.*, 2006, **74**, 045306.
35 P. E. de Jongh and D. Vanmaekelbergh, *Phys. Rev. Lett.*, 1996, **77**, 3427–3430.
36 N. G. Park, J. van de Lagemaat and A. J. Frank, *J. Phys. Chem. B*, 2000, **104**, 8989–8994.
37 L. M. Peter and K. G. U. Wijayantha, *Electrochem. Commun.*, 1999, **1**, 576–580.
38 N. Kopidakis, E. A. Schiff, N. G. Park, J. van de Lagemaat and A. J. Frank, *J. Phys. Chem. B*, 2000, **104**, 3930–3936.
39 F. Cao, G. Oskam, G. J. Meyer and P. C. Searson, *J. Phys. Chem.*, 1996, **100**, 17021–17027.
40 F. K. Dolezalek, *Photoconductivity and Related Phenomena*, ed. J. Mort and D. M. Pei, Elsevier, Amsterdam, 1976, p. 27.
41 K. Zhu, N. R. Neale, A. Miedaner and A. J. Frank, *Nano Lett.*, 2006, **7**, 69–74.
42 B. H. Lee, M. Y. Song, S.-Y. Jang, S. M. Jo, S.-Y. Kwak and D. Y. Kim, *J. Phys. Chem.C*, 2009, **113**, 21453–21457.
43 J. E. Kroeze, N. Hirata, L. Schmidt-Mende, C. Orizu, S. D. Ogier, K. Carr, M. Grätzel and J. R. Durrant, *Adv. Funct. Mater.*, 2006, **16**, 1832–1838.
44 L. Yang, U. B. Cappel, E. L. Unger, M. Karlsson, K. M. Karlsson, E. Gabrielsson, L. Sun, G. Boschloo, A. Hagfeldt and E. M. J. Johansson, *Phys. Chem. Chem. Phys.*, 2012, **14**, 779–789.
45 H. Sirringhaus, P. J. Brown, R. H. Friend, M. M. Nielsen, K. Bechgaard, B. M. W. Langeveld-Voss, A. J. H. Spiering, R. A. J. Janssen, E. W. Meijer, P. Herwig and D. M. de Leeuw, *Nature*, 1999, **401**, 685–688.
46 S. Ito, P. Chen, P. Comte, M. K. Nazeeruddin, P. Liska, P. Péchy and M. Grätzel, *Progress in Photovoltaics: Research and Applications*, 2007, **15**, 603–612.
47 T. Horiuchi, H. Miura, K. Sumioka and S. Uchida, *J. Am. Chem. Soc.*, 2004, **126**, 12218–12219.
48 B. C. O'Regan and F. Lenzmann, *J. Phys. Chem. B*, 2004, **108**, 4342–4350.
49 P. Docampo, S. Guldin, M. Stefik, P. Tiwana, M. C. Orilall, S. Huttner, H. Sai, U. Wiesner, U. Steiner and H. J. Snaith, *Adv. Funct. Mater.*, 2010, **20**, 1787–1796.
50 J. Bisquert, A. Zaban, M. Greenshtein and I. Mora-Sera, *J. Am. Chem. Soc.*, 2004, **126**, 13550–13559.
51 J. van de Lagemaat and A. J. Frank, *J. Phys. Chem. B*, 2001, **105**, 11194–11205.